Available online at www.sciencedirect.com
SCIENCE DIRECT®
International Journal of Solids and Structures 42 (2005) 2265–2285
INTERNATIONAL JOURNAL OF SOLIDS and STRUCTURES
www.elsevier.com/locate/ijsolstr

Elastic model of an entangled network of interconnected fibres accounting for negative Poisson ratio behaviour and random triangulation

Francis Delannay *

Département des Sciences des matériaux et des procédés, PCIM, Université catholique de Louvain, Place Sainte Barbe 2, B-1348 Louvain-la-Neuve, Belgium

Received 18 March 2004; received in revised form 14 September 2004
Available online 27 October 2004

Abstract

A model is designed for predicting the elastic constants of a random planar network of interconnected fibres while accounting for two features of such networks: negative Poisson ratio behaviour and random triangulation. The model is based on a periodic network involving both plates and fibres segments, with possibility of reentrant cell shapes. The plates are intended to represent the effect of triangulation. Bounds for the elastic constants are obtained by calculating volume weighted averages of the elastic properties for periodic networks characterised by a uniform distribution of in-plane fibre orientations. Predictions are derived for the dependence of the in-plane Young's modulus, out-of-plane Young's modulus, and in-plane shear modulus on out-of-plane fibre orientation for a fibre volume fraction of 0.20. These predictions are assessed by reference to experimental results for transversely isotropic networks, with very low average out-of-plane fibre orientation, made by sintering compressed mats of stainless steel fibres. A comparison is also made with the predictions of a model for truss lattice core, which is liable to represent the case of a fully triangulated network.

Keywords: Foams; Fibres; Elastic behaviour; Poisson ratio; Anisotropy

1. Introduction

Solid networks made of an assembly of interconnected fibres tightly bonded at the fibre contact points constitute a particular type of open-celled "cellular" material. In the case of metallic fibres, interconnected

* Tel.: +32 10 47 24 26; fax: +32 10 47 40 28.
E-mail address: delannay@pcim.ucl.ac.be

0020-7683/$ - see front matter © 2004 Elsevier Ltd. All rights reserved.
doi:10.1016/j.ijsolstr.2004.09.011

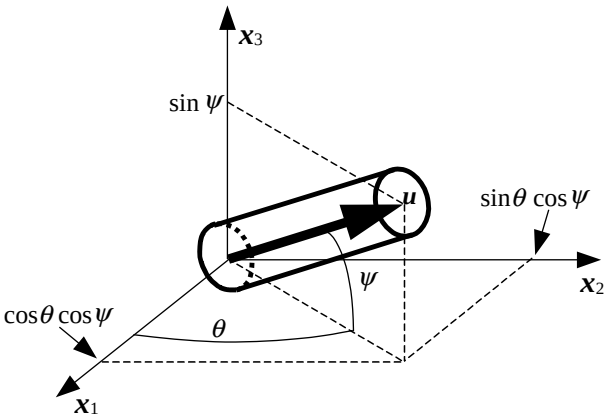

Fig. 1. Orientation of a fibre segment with respect to the co-ordinate axes. For a random planar network, plane (x_1, x_2) is taken as the plane of transverse isotropy ("in-plane" directions) and direction x_3 as the isotropy axis ("out-of-plane" direction).

networks with controlled fibre volume fraction and orientation distribution can be prepared by sintering felts of fibres. Such metallic fibre networks could find application as core material for lightweight sandwich plates combining both structural and heat transfer properties. For a given fibre volume fraction, V_f, these properties strongly depend on the anisotropy of the fibre orientation distribution. Faithful models for predicting the elastic behaviour of networks of interconnected fibres are needed for the design of sandwich cores with optimised properties. The potentially very high anisotropy and the fact that no elementary polyhedron constituting a "cell" can be defined render fibre networks quite different from cellular solids in general.

The model developed in the present paper is constructed and assessed by reference to experimental results for transversely isotropic, random fibre networks made by sintering compressed mats of 12 μm diameter fibres of stainless steel 316L with $V_f = 0.20$ (a product of N.V. Bekaert S.A., Belgium). Measurement of the whole set of five independent elastic constants ensuing from the transversely isotropic symmetry of this reference material was reported by Delannay and Clyne (1999). As sketched in Fig. 1, we define the orientation of a fibre segment by the spherical coordinate angles ψ and θ with respect to a right handed Cartesian system of axes. Plane (x_1, x_2) is the plane of transverse isotropy of the network ("in-plane" directions) and direction x_3 is the axis of symmetry ("out-of-plane" direction). Observation by scanning electron microscopy indicated that, in the considered reference material, (i) the distribution of the "out-of-plane" angles ψ is limited to small angles (77% of the fibres were found to be in the range $0^\circ \leqslant \psi \leqslant 10^\circ$) and (ii) the average distance L between two nodes along a fibre is somewhat less than 10 fibre diameters D (Delincé and Delannay, 2004). Denoting E the Young's modulus of the fibres, the non-dimensional in-plane modulus E_1/E was $\approx 35 \times 10^{-3}$, the out-of-plane modulus E_3/E was $\approx 1.1 \times 10^{-3}$ and the in-plane shear modulus G_{13}/E was $\approx 1.2 \times 10^{-3}$ (Delannay and Clyne, 1999). Strikingly, a quite large negative Poisson ratio $\nu_{13} \approx -1.7$ was measured in the out-of-plane direction.

Recently, Delincé and Delannay (2004) presented a model for predicting the dependence of the stiffness matrix, C_{ij} or compliance matrix, S_{ij} (as defined by Nye, 1985) of random planar fibre networks on fibre volume fraction and fibre orientation distribution. The elastic behaviour was analysed by considering the periodic network sketched in Fig. 2. This network involves only rings of six interconnected fibre segments. All segments have the same length and exhibit only two out-of-plane orientations $+\psi$ and $-\psi$ and two in-plane orientations θ_1 and θ_2. That model is unable to account for the possibility of negative Poisson ratio behaviour, which is a major feature of the tests carried out on the reference material. Indeed, although other structural mechanisms can bring about negative Poisson ratio (Rothenburg et al., 1991;

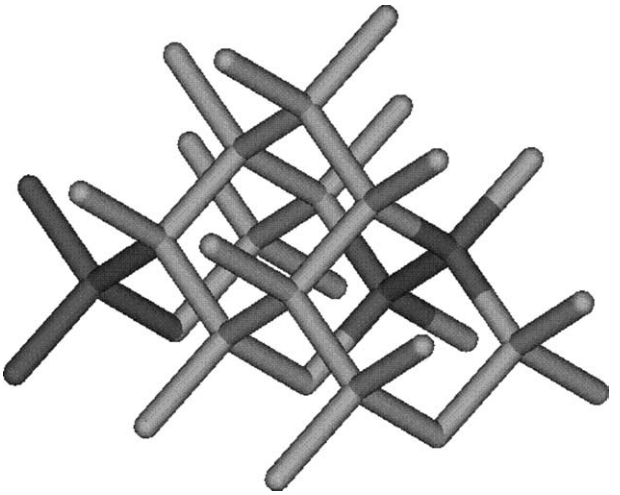

Fig. 2. Periodic network used in the model of Delincé and Delannay (2004).

Milton, 1992), negative Poisson ratio in cellular solids is commonly considered to result from reentrant cell shapes (Schajer and Robertson, 1974; Kolpakov, 1985; Lakes, 1987, 1991; Friis et al., 1988; Evans et al., 1994; Gibson and Ashby, 1997; Overaker et al., 1998a,b).

Although the trends revealed by the model of Delincé and Delannay (2004) appeared sound from the mechanical point of view, the model predictions were found to underestimate the elastic constants measured for the reference material. This too large compliance was ascribed to the fact that the model did not consider the presence of triangles formed by three mutually intersecting fibres. Such a triangulation effect increases the network stiffness because bending of the fibres is prevented in the direction parallel to the plane of the triangles. Intuitively, the degree of triangulation is expected to be larger when fibres are more parallel to one another, i.e. when the average out-of-plane angle ψ is smaller. In Appendix A, a simple model is used for demonstrating that, indeed, the magnitude of the in-plane modulus E_1 measured for the reference fibre network cannot be accounted for without considering the effect of triangulation.

The objective of the present paper is to develop a new model liable to circumvent the limitations of the model of Delincé and Delannay (2004). This new model involves (i) the possibility of reentrant shapes that could bring about negative Poisson ratio behaviour, and (ii) the presence of plates intended to reproduce the effect of triangles of fibres. As for the model introduced by Delincé and Delannay (2004), bounds for the components of the stiffness matrix, C_{ij} or compliance matrix, S_{ij} are derived using Voigt and Reuss averaging procedures. The results of the two models are compared to predictions for truss lattices and evaluated with respect to the experimental data for the reference material.

2. Model

2.1. Geometry of the periodic model networks

Fig. 3a illustrates the architecture of a model network of fibres designed for exhibiting the requested behaviour. The difference with respect to the network of Fig. 2 is that the network combines rings of 6 fibre segments together with equilateral triangles of 3 fibre segments. The segments forming the triangles are parallel to the plane of transverse isotropy ($\psi = 0$) whereas the other segments present two symmetrical out-of-plane

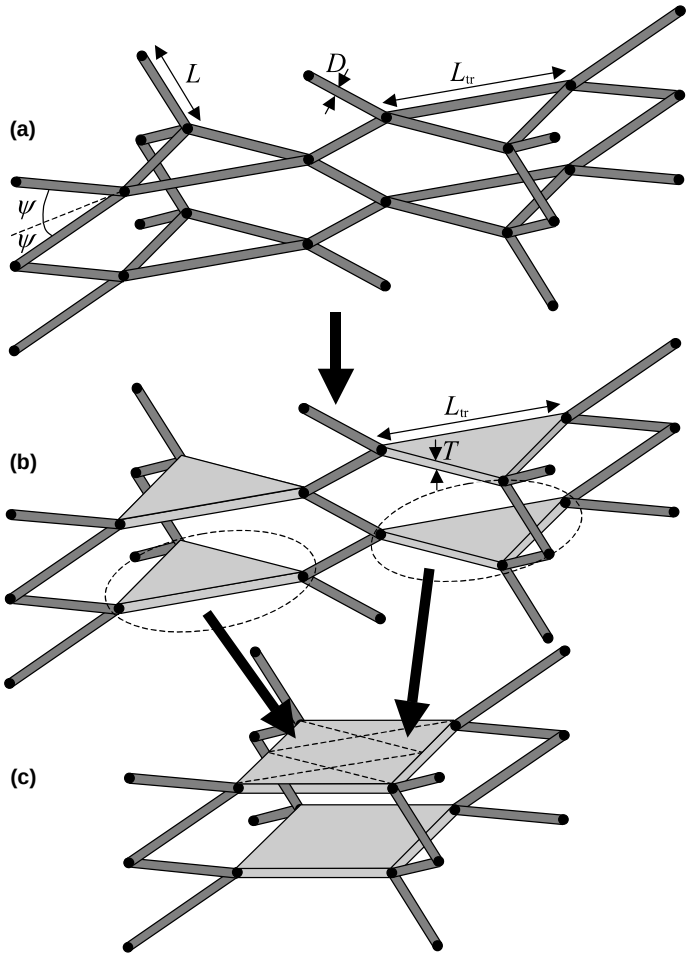

Fig. 3. (a) Network combining rings of 6 fibres segments and equilateral triangles of 3 fibres segments. The segments forming the triangles are parallel to the plane of transverse isotropy ($\psi = 0$) whereas the other segments present two symmetrical out-of-plane orientation angles $+\psi$ and $-\psi$ and three different in-plane orientation angles; (b) same network with triangles of fibres substituted by triangular plates; (c) simplified model obtained by merging two triangular plates to form a rectangular plate.

orientation angles $+\psi$ and $-\psi$. Three different in-plane orientation angles θ_1, θ_2 and θ_3 (not specified on the figure) are given to the three pairs of segments meeting at the corners of the triangles. All fibres have the same diameter, D. The segments forming the equilateral triangles have a length, L_{tr} which differs from the length, L, of the other segments. The ratio L_{tr}/L is an adjustable parameter allowing the tuning of the degree of triangulation in the network. It can easily be realised that, in addition to accounting for triangulation, the network of Fig. 3a can present reentrant shapes liable to bring about negative Poisson ratio behaviour.

Fig. 3b presents a similar network design in which each group of three fibre segments forming a triangle has been substituted by a triangular plate. This network presents essentially the same mechanical properties as the original one if the plate thickness, T, is chosen to be such that the plate volume is equal to the volume of the three original fibre segments (i.e., $T = \sqrt{3}\pi D^2/L_{tr}$). Indeed, as for triangles of fibres, only stretching and shearing contribute to the in-plane deformation of plates, whereas bending governs the out-of-plane deformation (the shearing contribution being negligible if the ratio L_{tr}/T is large enough).

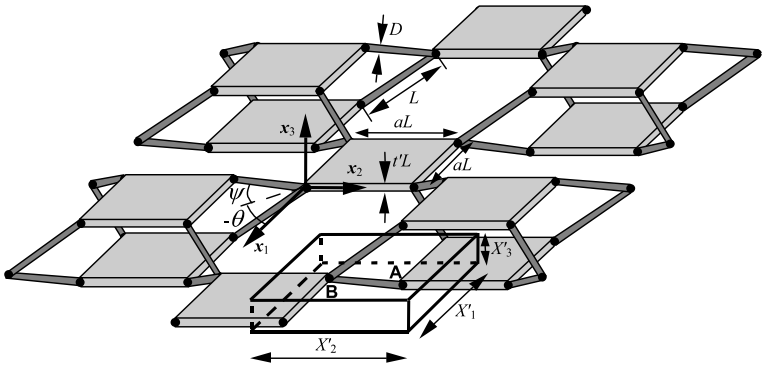

Fig. 4. First type of periodic model used for predicting the elastic properties of a random planar network of interconnected fibres.

The analysis of the elastic behaviour of such a periodic network containing triangular plates with two different orientations and fibres segments with three different in-plane orientation angles θ is fairly complex. In order to simplify this analysis, we propose to substitute this network by a network in which pairs of triangular plates with different orientations are merged to form a rectangular plate, as represented in Fig. 3c. In this way, the fibre segments present only two different in-plane orientation angles θ (as for the model of Fig. 2). As detailed in Sections 2.2 and 2.3 hereafter the length and width of the plates can be chosen such as to comply with the spatial distribution of the nodes in the network whereas their thickness can be chosen such as to comply with the solid volume fraction V_f. The basic assumption is that the mechanical behaviours of the networks of Fig. 3b and c are qualitatively similar. It will be shown that, indeed, the dependence on ψ of the elastic properties predicted for a model based on Fig. 3c follows a similar trend as for the model of Fig. 2. In order to allow triangulation to operate in different plane directions, two different periodic model networks based on Fig. 3c have to be considered (a preliminary report on this modelling approach was given by Delannay, 1998).

The first periodic model network to be considered is sketched in Fig. 4. The model directly derives from Fig. 3c: it consists of a periodic arrangement of fibre segments of length L oriented along the four directions $(+\theta,+\psi)$, $(+\theta,-\psi)$, $(-\theta,+\psi)$ (the latter being the orientation of the fibre segment specified in Fig. 4), and $(-\theta,-\psi)$. These fibre segments are connected to square plates of size $(aL \times aL \times t'L)$ perpendicular to axis $\boldsymbol{x}_3$. The values of θ and ψ may be chosen anywhere in the ranges $-\pi \leqslant \theta \leqslant \pi$ and $0 \leqslant \psi \leqslant \pi/2$. The major feature of this periodic network is that it expands along $\boldsymbol{x}_3$ under tension loading along $\boldsymbol{x}_2$ when $-\pi < \theta < 0$ and under tension loading along $\boldsymbol{x}_1$ when $\theta < -\pi/2$ or $\theta > \pi/2$: negative Poisson ratio behaviour is thus allowed in the out-of-plane direction (as observed for the reference material). The values to be chosen for the size parameters a and t' of the plates are discussed in Sections 2.2 and 2.3 hereafter. Obviously, the larger a and t', the larger the triangulation contribution to the network stiffness.

In order to account for other possible triangulation planes, it is necessary to consider also the second type of model illustrated in Fig. 5. It consists of the same regular arrangement of fibre segments of length L oriented along the four directions $(+\theta,+\psi)$, $(+\theta,-\psi)$, $(-\theta,+\psi)$ (the latter being the orientation of the fibre indicated in Fig. 5), and $(-\theta,-\psi)$, but these fibre segments are now connected to rectangular plates of size $(aL \times cL \times t''L)$ perpendicular to axis $\boldsymbol{x}_1$. In this case, the values of θ and ψ may be chosen anywhere in the ranges $-\pi/2 \leqslant \theta \leqslant \pi/2$ and $-\pi/2 \leqslant \psi \leqslant \pi/2$. Referring to Fig. 5, one notices that the network expands along $\boldsymbol{x}_1$ under tension loading along $\boldsymbol{x}_2$ when $-\pi/2 < \theta < 0$ and under tension loading along $\boldsymbol{x}_3$ when $-\pi/2 < \psi < 0$. The plates account for triangulation in the plane perpendicular to $\boldsymbol{x}_1$. The values to be chosen for the size parameters a, c, and t'' are discussed in Sections 2.2 and 2.3.

As detailed in Section 2.5, the procedure will consist in calculating the bounds for the elastic properties of a "composite" combining periodic networks such as illustrated in Figs. 4 or 5 with ψ and θ distributed in

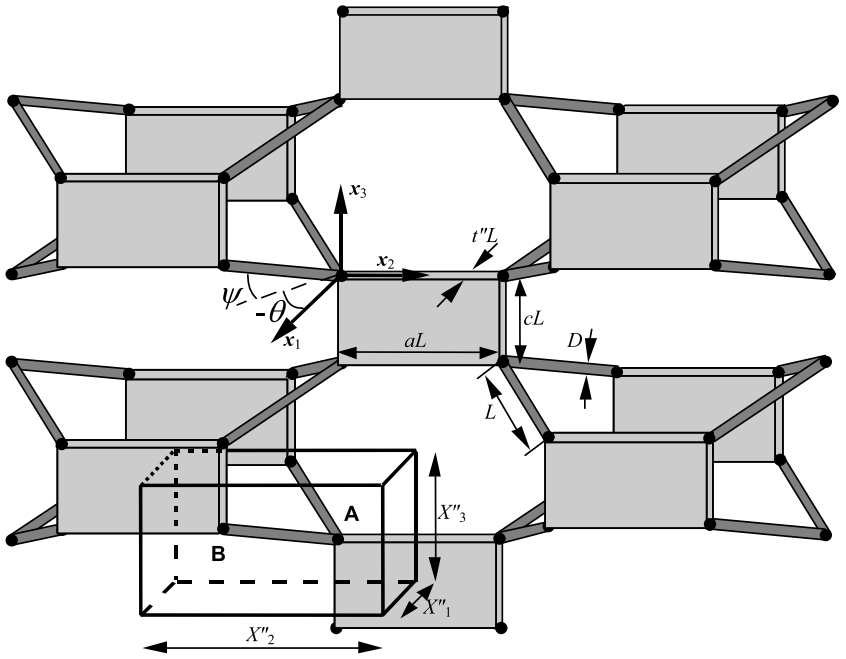

Fig. 5. Second type of periodic model used for predicting the elastic properties of a random planar network of sintered fibres.

their admissible ranges. As the original periodic networks present orthotropic symmetry, the results of this averaging procedure keep complying with orthotropy. In order to retrieve the transverse isotropy of the actual networks, these results will then be averaged with respect to all rotations around the $\boldsymbol{x}_3$ axis. Finally, in order to account for the different planes in which triangulation can exist, averages will be taken of the results for plates perpendicular to $\boldsymbol{x}_1$, $\boldsymbol{x}_2$ and $\boldsymbol{x}_3$. As $\boldsymbol{x}_1$ and $\boldsymbol{x}_2$ are equivalent, this means that the model of Fig. 5 will be given twice the weight of the model of Fig. 4.

2.2. Plate size parameters a and c

As proposed by Delincé and Delannay (2004), the architecture of any particular random planar fibre network may be characterised by a node distribution function $F_{\mathrm{d}L_{\mathrm{fs}}\mathrm{d}\theta\mathrm{d}\psi}(L_{\mathrm{fs}},\theta,\psi)$ which expresses the probability that a fibre segment originating from a particular node meets another fibre at another node located at a distance between L_{fs} and $L_{\mathrm{fs}}+\mathrm{d}L_{\mathrm{fs}}$ in a direction included within the solid angle between (θ,ψ) and $(\theta+\mathrm{d}\theta,\psi+\mathrm{d}\psi)$. For constructing the model networks, it makes sense to choose as length L of the fibre segments the average distance between two nodes connected by a fibre segment in the actual network. This average can be calculated as

$$L=\int_{L_{\mathrm{fs}}=0}^{\infty}\int_{\psi=0}^{\pi/2}\int_{\theta=0}^{2\pi}F_{\mathrm{d}L_{\mathrm{fs}}\,\mathrm{d}\theta\,\mathrm{d}\psi}(L_{\mathrm{fs}},\theta,\psi)L_{\mathrm{fs}}\cos\psi\,\mathrm{d}L_{\mathrm{fs}}\,\mathrm{d}\theta\,\mathrm{d}\psi. \tag{1}$$

The distribution $F_{\mathrm{d}\psi}(\psi)$ of the relative orientations of pairs of nodes connected by a fibre segment is obtained as

$$F_{\mathrm{d}\psi}(\psi)=\frac{1}{L}\int_{L_{\mathrm{fs}}=0}^{\infty}\int_{\theta=0}^{2\pi}F_{\mathrm{d}L_{\mathrm{fs}}\,\mathrm{d}\theta\,\mathrm{d}\psi}(L_{\mathrm{fs}},\theta,\psi)L_{\mathrm{fs}}\cos\psi\,\mathrm{d}L_{\mathrm{fs}}\,\mathrm{d}\theta. \tag{2}$$

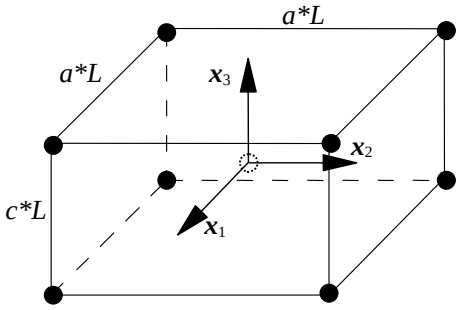

Fig. 6. Unit cell representing the average distribution of the nodes in the network.

$F_{d\psi}(\psi)$ is similar, but not exactly identical, to the fibre orientation distribution. Indeed, in actual networks, fibres are not perfectly straight between nodes and the contact points constituting the nodes are not along the fibre axis.

In order to find the ratio a/c of the plate sizes which best complies with the architecture of the actual random planar network to be modelled, we propose to determine the parameters, denoted a^*L and c^*L, of a body-centred tetragonal lattice which would best represent the distribution of the nodes in the network. Let us, for this purpose, locate the origin of the coordinates system of axes at a particular node, as sketched in Fig. 6. The eight most probable positions of the nodes closest to this particular one are at the apexes of a tetragonal unit cell, the parameters, a^*L and c^*L, of which are equal to twice the averages of the projections, on the three coordinate axes, of a fibre segment of length L originating from the node at the origin. For a transversely isotropic network, a^* and c^* are obtained as

$$a^* = 2\frac{\int_{\psi=0}^{\pi/2}\int_{\theta=0}^{\pi/2} F_{d\psi}(\psi)\cos\theta\cos\psi\,d\theta\,d\psi}{\int_{\psi=0}^{\pi/2}\int_{\theta=0}^{\pi/2} F_{d\psi}(\psi)\,d\theta\,d\psi} = \frac{4}{\pi}\int_{\psi=0}^{\pi/2} F_{d\psi}(\psi)\cos\psi\,d\psi \tag{3}$$

and

$$c^* = 2\frac{\int_{\psi=0}^{\pi/2} F_{d\psi}(\psi)\sin\psi\,d\psi}{\int_{\psi=0}^{\pi/2} F_{d\psi}(\psi)\,d\psi} = 2\int_{\psi=0}^{\pi/2} F_{d\psi}(\psi)\sin\psi\,d\psi. \tag{4}$$

As only 4 fibre segments (i.e. two fibres crossing one another) meet at the node located at the centre of the unit cell, the latter would be connected to only four among the eight nodes of which the average positions are at the apexes of the unit cell. It can be noticed that, with the definitions (3) and (4) of a^* and c^*, the distance between the origin and the unit cell apexes is not equal to L.

The parameters a^* and c^* thus depend only on the distribution $F_{d\psi}(\psi)$. The simplest case consists in considering that all fibres have the same orientation ψ (i.e. $F_{d\psi}(\psi) = \delta(\psi)$ where $\delta(\psi)$ is the Dirac function). In that case, relations (3) and (4) yield

$$a^* = \frac{4}{\pi}\cos\psi \tag{5}$$

and

$$c^* = 2\sin\psi. \tag{6}$$

A more realistic case would be a network in which the distribution $F_{d\psi}(\psi)$ is uniform from $\psi = 0$ up to a maximum $\psi = \psi_m$ beyond which it is zero. Relations (3) and (4) yield in that case

$$a^* = \frac{2}{\pi \sin\psi_m}\left(\psi_m + \frac{\sin 2\psi_m}{2}\right) \tag{7}$$

and

$$c^* = \sin\psi_m. \tag{8}$$

a^* and c^* can be derived in a similar way for any other distribution $F_{d\psi}(\psi)$.

Two characteristics of fibre networks can be quite easily measured experimentally: the fibre volume fraction V_f and the fibre orientation distribution, which we can take as representative of $F_{d\psi}(\psi)$ (Delincé and Delannay, 2004). In contrast, it is very difficult to measure the average distance L between two nodes. However, if one assumes that the fibre cross sections are circular with constant diameter, D and that the fibre segments are straight between nodes, L is a function only of V_f and $F_{d\psi}(\psi)$. Indeed, each unit cell represented in Fig. 6 contains in average four fibres segments of length L. Hence, neglecting the volume of the node itself, the fibre volume fraction writes

$$V_f = 4L\frac{\pi D^2}{4}\frac{1}{L^3 a^{*2} c^*} \tag{9}$$

or

$$\frac{D}{L} = \frac{1}{l} = \sqrt{\frac{V_f a^{*2} c^*}{\pi}}. \tag{10}$$

The dependence of l on $F_{d\psi}(\psi)$ expresses through a^* and c^*.

In order to get the best correspondence between the periodic model networks of Figs. 4 and 5 and the actual network architecture, it makes sense to take $a = ka^*$ and $c = kc^*$ with the same proportionality factor k. The next issue is the choice of the value to be given to k in order to correctly represent the degree of triangulation in the network: the larger the factor k, the larger the triangulation, hence the larger the network stiffness. In the lack of pertinent a priori argument for orienting the choice of k, k remains an adjustable parameter to be identified a posteriori by comparing model predictions to experimental data. Although the model of the present paper can be developed for any value of k (except for the limitation mentioned in Section 2.3), all computational results presented in the present paper were obtained with $k = 1$, i.e. by taking $a = a^*$ and $c = c^*$.

2.3. Plate thickness parameters t' and t''

The thickness parameters t' and t'' can be derived by considering in Figs. 4 and 5 the representative volume elements (RVE) of size ($X'1 \times X'2 \times X'3$) and ($X''1 \times X''2 \times X''3$), respectively, around the fibre segment AB. In Fig. 4, the volume $V'_{RVE}(\theta,\psi)$ of the RVE writes

$$V'_{RVE}(\theta,\psi) = L^3(a + \cos\psi\sin\theta)(a + \cos\psi\cos\theta)\sin\psi, \tag{11}$$

whereas, in Fig. 5, the volume V''_{RVE} of the RVE writes

$$V''_{RVE}(\theta,\psi) = L^3(a + \cos\psi\sin\theta)(c + \sin\psi)\cos\psi\cos\theta. \tag{12}$$

The actual random network behaves like a "composite" network combining all networks with angles θ and ψ distributed according to the actual fibre orientation distribution. The volume fraction V_f of solid can thus be calculated by noticing that each RVE contains one fibre segment and 1/4 of the volume of a plate. For example, for the network of Fig. 5,

$$V_f = \frac{1}{\langle V''_{RVE}\rangle}\left(\frac{t''acL^3}{4} + \frac{\pi D^2 L}{4}\right), \tag{13}$$

where $\langle V''_{\mathrm{RVE}}\rangle$ denotes the average RVE volume in the composite network. In the case of random planar symmetry, this average volume can be derived from the orientation distribution function $F_{\mathrm{d}\psi}(\psi)$ as

$$\langle V''_{\mathrm{RVE}}\rangle = \frac{\int_{\psi=-\pi/2}^{\pi/2}\int_{\theta=-\pi/2}^{\pi/2} V''_{\mathrm{RVE}}(\theta,\psi)F_{\mathrm{d}\psi}(\psi)\,\mathrm{d}\theta\,\mathrm{d}\psi}{\int_{\psi=-\pi/2}^{\pi/2}\int_{\theta=-\pi/2}^{\pi/2} F_{\mathrm{d}\psi}(\psi)\,\mathrm{d}\theta\,\mathrm{d}\psi}. \tag{14}$$

For the network of Fig. 4, the average RVE volume $\langle V'_{\mathrm{RVE}}\rangle$ is obtained using a similar relation as (14), except that the integration is then carried out over the ranges $-\pi \leqslant \theta \leqslant \pi$ and $0 \leqslant \psi \leqslant \pi/2$. It may be verified that, combining (11) or (12) with (14), the same result is obtained whatever the fibre orientation distribution $F(\psi)$:

$$\langle V'_{\mathrm{RVE}}\rangle = \langle V''_{\mathrm{RVE}}\rangle = \tfrac{1}{2}L^3a^2c. \tag{15}$$

The model breaks down if a ($=ka^*$) and c ($=kc^*$) are taken too small: indeed, combination of (13) and (15) shows that t' and t'' decrease with decreasing k and they should be given a negative value below a certain value of k.

In the following of this paper, we consider only the choice $a = a^*$ and $c = c^*$ ($k = 1$). For this particular case, relations (10), (13), and (15) yield, for the network of Fig. 4,

$$t' = V_{\mathrm{f}}c \tag{16}$$

and, for the network of Fig. 5,

$$t'' = V_{\mathrm{f}}a. \tag{17}$$

Combining (16) and (17) with (9) shows that, whatever the distribution $F_{\mathrm{d}\psi}(\psi)$, the volume of each plate is then equal to the volume of 4 fibre segments of length L.

2.4. Expression of compliance matrix components S_{ij}

The method used for the analysis of the elastic behaviour of the periodic networks of Figs. 4 and 5 is an extension to the 3D case of the method used by Gibson and Ashby (1997) for the analysis the elastic properties of 2D honeycombs (the present paper is limited to the study of the elastic behaviour but the two model networks of Figs. 4 and 5 could also be used for evaluating the resistance of a random fibre network to buckling or yielding).

As the two periodic models present orthotropic symmetry, their compliance matrix involves nine independent components S_{ij} (Nye, 1985), which will be denoted S'_{ij} and S''_{ij} for the cases of Figs. 4 and 5, respectively. Analytical expressions for these components have been derived by considering:

(i) for the fibre segments, the deformations in bending and stretching but not in shearing;
(ii) for the plates, the in-plane deformations in stretching and shearing and the out-of-plane deformations in bending but not in shearing;
(iii) no relative rotation of the fibres and plates at the nodes.

Accounting for stretching of the beams and of the plates was necessary in order to avoid obtaining infinite stiffness at the limits of the θ, ψ ranges where fibres and plates align with the loading directions. Using relations (7)–(12) together with relations (18) and (19), it may be verified that, for networks with volume fraction $V_{\mathrm{f}} \leqslant 0.2$, the aspect ratio of the fibres and plates is always large enough for neglecting shearing in comparison to bending for the transverse deflection of the beams and for the out-of-plane deflection of the plates. Approximation (iii) may be the most questionable as, if the contact nodes are not sufficiently

welded (which depends on the sintering conditions used for consolidating the network), the stiffness of the connections between the fibres can be not large enough as to prevent some relative fibre rotation.

The expressions for the S'_{ij} and S''_{ij} are given in Tables 1 and 2. The procedure for deriving these expressions is presented in Appendix B. For symmetry reasons, the elastic response of the models under tension or compression in directions parallel to the reference axes are completely specified by the behaviour of the representative volume element (RVE) defined around the fibre segment AB in Figs. 4 and 5. The computation

Table 1
Non-dimensional compliance matrix components $S'_{ij}E$ (using $A = \frac{16l^4}{3\pi}$) for the periodic model network of Fig. 4

$$S'_{11}E = A(a+\cos\psi\sin\theta)\sin\psi(a+\cos\psi\cos\theta)^{-1}\left[1+\tfrac{3}{4}\tfrac{a^2}{l^2}-\left(1-\tfrac{3}{4l^2}\right)\cos^2\psi\cos^2\theta\right]$$

$$S'_{12}E = -A\sin\psi\left[\nu\tfrac{3}{4}\tfrac{a^2}{l^2}+\left(1-\tfrac{3}{4l^2}\right)\cos 2\psi\sin\theta\cos\theta\right]$$

$$S'_{13}E = -A(a+\cos\psi\sin\theta)\cos\psi\sin\psi\cos\theta\left(1-\tfrac{3}{4l^2}\right)$$

$$S'_{22}E = A(a+\cos\psi\cos\theta)\sin\psi(a+\cos\psi\sin\theta)^{-1}\left[1+\tfrac{3}{4}\tfrac{a^2}{l^2}-\left(1-\tfrac{3}{4l^2}\right)\cos^2\psi\sin^2\theta\right]$$

$$S'_{23}E = -A(a+\cos\psi\cos\theta)\cos\psi\sin\psi\sin\theta\left(1-\tfrac{3}{4l^2}\right)$$

$$S'_{33}E = A(a+\cos\psi\sin\theta)(a+\cos\psi\cos\theta)(\sin\psi)^{-1}\left[1-\left(1-\tfrac{3}{4l^2}\right)\sin^2\psi\right]$$

$$S'_{66}E = A\frac{(a+\cos\psi\cos\theta)\sin\psi}{a+\cos\psi\sin\theta}\left\{\frac{a^2\cos^2\psi(\cos\theta-\sin\theta)^2}{(a+\cos\psi\sin\theta)^2}+2\frac{a^2}{l^2}+\frac{3}{4l^2}\right.$$
$$\left.\times\left[\cos^2\psi\cos^2\theta+\frac{\cos^2\psi\cos\theta\sin\theta(2a+\cos\psi\sin\theta)}{a+\cos\psi\cos\theta}+\frac{a(a+\cos\psi\sin\theta)\cos^2\psi\sin^2\theta}{(a+\cos y\cos\theta)^2}\right]\right\}$$

$$S'_{44}E = S'_{55}E = A\frac{(a+\cos\psi\sin\theta)\sin\psi}{a+\cos\psi\cos\theta}\left\{a^2+\frac{3a^6}{4\pi V_f c}+\frac{3}{4l^2}\left[\sin^2\psi+\cos\theta\cos\psi(2a+\cos\theta\cos\psi)+\frac{a(a+\cos\psi\cos\theta)\cos^2\psi\sin^2\theta}{\sin^2\psi}\right]\right\}$$

Table 2
Non-dimensional compliance matrix components $S''_{ij}E$ (using $A = \frac{16l^4}{3\pi}$) for the periodic model network of Fig. 5

$$S''_{11}E = A(a+\cos\psi\sin\theta)(c+\sin\psi)(\cos\psi\cos\theta)^{-1}\left[1-\left(1-\tfrac{3}{4l^2}\right)\cos^2\psi\cos^2\theta\right]$$

$$S''_{12}E = -A\left(1-\tfrac{3}{4l^2}\right)(c+\sin\psi)\cos^2\psi\cos\theta\sin\theta$$

$$S''_{13}E = -A\left(1-\tfrac{3}{4l^2}\right)(a+\cos\psi\sin\theta)\sin\psi\cos\psi\cos\theta$$

$$S''_{22}E = A(c+\sin\psi)\cos\psi\cos\theta(a+\cos\psi\sin\theta)^{-1}\left[1+\tfrac{3}{4}\tfrac{a^2}{l^2}-\left(1-\tfrac{3}{4l^2}\right)\cos^2\psi\sin^2\theta\right]$$

$$S''_{23}E = -A\cos\psi\cos\theta\left[\nu\tfrac{3}{4}\tfrac{ac}{l^2}+\left(1-\tfrac{3}{4l^2}\right)\cos\psi\sin\psi\sin\theta\right]$$

$$S''_{33}E = A(a+\cos\psi\sin\theta)\cos\psi\cos\theta(c+\sin\psi)^{-1}\left[1+\tfrac{3}{4}\tfrac{c^2}{l^2}-\left(1-\tfrac{3}{4l^2}\right)\sin^2\psi\right]$$

$$S''_{66}E = A\frac{(c+\sin\psi)\cos\psi\cos\theta}{a+\cos\psi\sin\theta}\left\{a^2+\frac{3a^4c}{4\pi V_f}+\frac{3}{4l^2}\left[\cos^2\psi+2a\cos\psi\sin\theta+a(a+\cos\psi\sin\theta)\tan^2\theta\right]\right\}$$

$$S''_{55}E = A\frac{(a+\cos\psi\sin\theta)\cos\psi\cos\theta}{c+\sin\psi}\left\{c^2+\frac{3c^5}{4\pi V_f}+\frac{3}{4l^2}\left[\cos^2\psi\sin^2\theta+\sin\psi(2c+\sin\psi)+\frac{c(c+\sin\psi)\tan^2\psi}{\cos^2\theta}\right]\right\}$$

$$S''_{44}E = A\frac{(a+\cos\psi\sin\theta)\cos\psi\cos\theta}{c+\sin\psi}\left\{\frac{(c\cos\psi\sin\theta-a\sin\psi)^2}{(a+\cos\psi\sin\theta)^2}+2\frac{c^2}{l^2}+\frac{3}{4l^2}\right.$$
$$\left.\times\left[\cos^2\psi\sin^2\theta+\frac{\sin\psi(2c+\sin\psi)\cos\psi\sin\theta}{a+\cos\psi\sin\theta}+\frac{c(c+\sin\psi)\sin^2\psi}{(a+\cos\psi\sin\theta)^2}\right]\right\}$$

of the shear components S'_{44}, S'_{55}, S'_{66}, S''_{44}, S''_{55} and S''_{66} requires considering twice as large RVEs involving a pair of fibres. Using these expressions for S'_{ij} and S''_{ij}, the components C'_{ij} and C''_{ij} of the stiffness matrices are obtained using the standard procedure for the inversion of the compliance matrix (Nye, 1985).

2.5. Computation of Reuss and Voigt bounds

Following common practice (e.g. Mura, 1982; Gommers et al., 1996) and similarly as done by Delincé and Delannay (2004), bounds for the elastic constants of a random planar fibre network are obtained by calculating the Reuss and Voigt bounds for the elastic constants of a "composite" network made by combining periodic networks of the type of Figs. 4 and 5 presenting uniform distributions of the in-plane angle θ. In order to simplify computations, we have limited ourselves to the hypothetical case where all fibres have the same orientation ψ (i.e. $F_{\mathrm{d}\psi}(\psi) = \delta(\psi)$). This case allows to best capture the influence of the fibre orientation. In order to account for the volume of the nodes, the effective length along which the fibre segments represented in Figs. 4 and 5 deform has been taken in the computations as equal to $L-D$ rather than to L.

The procedure for obtaining the Reuss bound starts by computing the volume weighted averages, S'^{R}_{ij} and S''^{R}_{ij}, of the compliance matrix components S'_{ij} and S''_{ij}. For example, in the case of the model of Fig. 5, these averages write

$$S''^{\mathrm{R}}_{ij} = \frac{\int_{\theta=-\pi/2}^{\pi/2} [V''_{\mathrm{RVE}}(\theta,\psi) S''_{ij}(\theta,-\psi) + V''_{\mathrm{RVE}}(\theta,-\psi) S''_{ij}(\theta,-\psi)]\,\mathrm{d}\theta}{\int_{\theta=-\pi/2}^{\pi/2} [V''_{\mathrm{RVE}}(\theta,\psi) + V''_{\mathrm{RVE}}(\theta,-\psi)]\,\mathrm{d}\theta}. \tag{18}$$

Secondly, as the compliance matrices S'^{R}_{ij} and S''^{R}_{ij} correspond to networks with orthotropic symmetry, the Reuss bounds for the five independent stiffness components of a transversely isotropic network are derived by averaging the S'^{R}_{ij} and S''^{R}_{ij} components with respect to all directions perpendicular to the $\boldsymbol{x}_3$ axis. The relations to be used for that purpose were given in Table 2 of the paper of Delincé and Delannay (2004). Finally, an average is taken of the stiffness matrix components calculated for periodic network models with plates perpendicular to $\boldsymbol{x}_1$, $\boldsymbol{x}_2$ and $\boldsymbol{x}_3$. As $\boldsymbol{x}_1$ and $\boldsymbol{x}_2$ are equivalent, the weight to be given to the model of Fig. 5 is twice the weight to be given to the model of Fig. 4. Hence, we take, as the best representative Reuss bound, the average matrix

$$S^{\mathrm{R}}_{ij} = \frac{S'^{\mathrm{R}}_{ij} + 2S''^{\mathrm{R}}_{ij}}{3}. \tag{19}$$

The procedure for obtaining the Voigt bounds of the elastic constants is similar: it involves (i) the computation of the volume weighted averages, C'^{V}_{ij} and C''^{V}_{ij}, of the nine components of the compliance matrices C'_{ij} and C''_{ij} (derived from S'_{ij} and S''_{ij} using the standard procedure for the inversion of the compliance matrix), (ii) the translation of these 9 C'^{V}_{ij} and C''^{V}_{ij} components into the five components complying with transverse isotropy and (iii) the computation of C^{V}_{ij} similarly as in (19). Finally, the Voigt bounds S^{V}_{ij} of the compliance matrix are derived from the matrix C^{V}_{ij} by matrix inversion.

The Reuss and Voigt bounds E^{R}_1, E^{R}_3, and G^{R}_{13} and E^{V}_1, E^{V}_3, and G^{V}_{13} are directly obtained from the bounds S^{R}_{ij} and S^{V}_{ij} with $i=j$. The bounds for the Poisson ratios ν_{12} and ν_{13} are somewhat more complex as they derive from the fact that the two following conditions must be satisfied simultaneously (e.g. Gommers et al., 1996):

$$S^{\mathrm{R}}_{ij} - \sqrt{(S^{\mathrm{R}}_{ii} - S_{ii})(S^{\mathrm{R}}_{jj} - S_{jj})} \leqslant S_{ij} \leqslant S^{\mathrm{R}}_{ij} + \sqrt{(S^{\mathrm{R}}_{ii} - S_{ii})(S^{\mathrm{R}}_{jj} - S_{jj})} \tag{20}$$

and

$$S^{\mathrm{V}}_{ij} - \sqrt{(S_{ii} - S^{\mathrm{V}}_{ii})(S_{jj} - S^{\mathrm{V}}_{jj})} \leqslant S_{ij} \leqslant S^{\mathrm{V}}_{ij} + \sqrt{(S_{ii} - S^{\mathrm{V}}_{ii})(S_{jj} - S^{\mathrm{V}}_{jj})}. \tag{21}$$

3. Results and discussion

Fig. 7 presents the variation as a function of ψ of the Voigt and Reuss bounds for E_1, E_3 and G_{13} for a fibre volume fraction $V_f = 0.20$. The overall behaviour is strikingly similar to the results obtained by Delincé and Delannay (2004) using the model illustrated in Fig. 2. E_1 exhibits a broad maximum in the range $10^\circ \leqslant \psi \leqslant 50^\circ$ and a sharp decrease when ψ increases above 70°. E_3 presents very low values at low ψ and increases monotonously with ψ to reach a wide maximum when ψ exceeds 45°. G_{13} is predicted to present a wide maximum in the range $20^\circ < \psi < 50^\circ$. As shown for example by Gibson and Ashby (1997) or Ashby et al. (2000), G_{13} is the most important elastic constant to be considered for application of fibre networks as core of sandwich structures. However, as sandwich cores should also have sufficient transverse stiffness, i.e. sufficient E_3 the optimum design value of ψ would presumably be larger than 40°.

Fig. 8 compares the predictions of the model of Delincé and Delannay (2004) (denoted "model 1") and of this paper (denoted "model 2") for E_1, E_3 and G_{13}. For this comparison, the curves presented for the two models are the geometrical averages of the two calculated bounds, e.g. $E_1^{\text{average}} = \sqrt{E_1^{\text{Voigt}} E_1^{\text{Reuss}}}$. Geometrical averages can be considered as most representative of the predictions because (i), in both models, no geometrical argument can be invoked to justify that the actual network behaviour should be closer to either of the two bounds and (ii) geometrical averaging yields the same average value when derived from stiffness

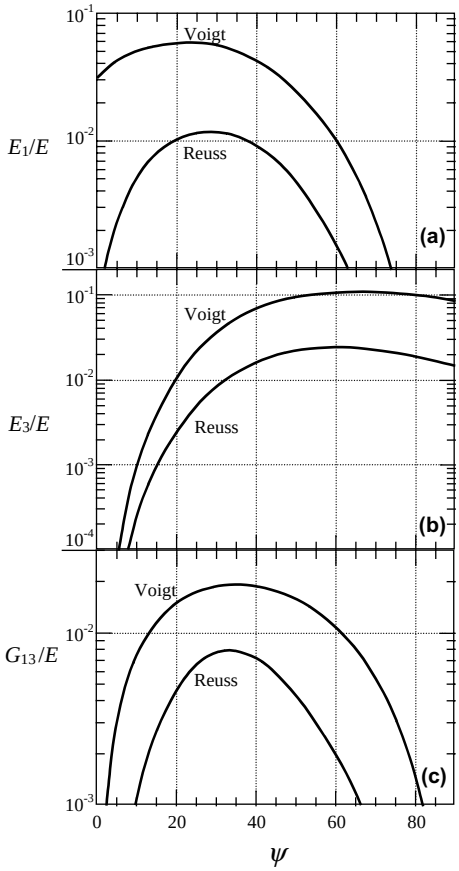

Fig. 7. Variation as a function of ψ of the Voigt and Reuss bounds for E_1, E_3 and G_{13} for a fibre volume fraction $V_f = 0.20$.

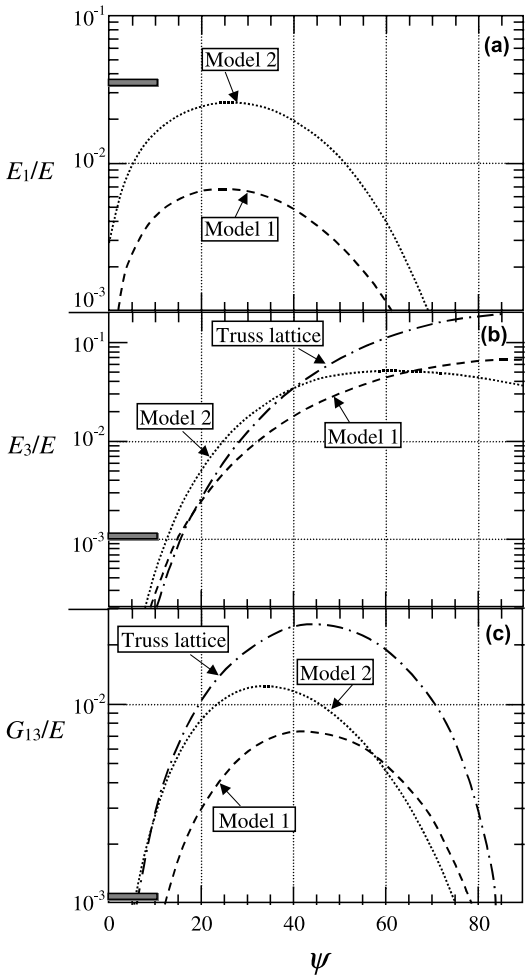

Fig. 8. Comparison of the geometrical averages of the bounds predicted by the model of Delincé and Delannay ("model 1") and of this paper ("model 2") for E_1, E_3 and G_{13} The three rectangles in grey scale locate the experimental values. The dot-dashed curves are the values of E_3 and G_{13} for truss lattices, as expressed by relations (22) and (23).

or compliance. The experimental values are represented in Fig. 8 by rectangles in grey scale. As anticipated, owing to the triangulation brought about by the plates, the present model (model 2) is generally stiffer than model 1 (except for E_3 at $\psi > 65^\circ$ and for G_{13} at $\psi > 55^\circ$). For E_1 whereas the trends for the dependence on ψ are remarkably similar for the two models, the predictions of model 2 are larger by a factor of about 4. Still, the prediction of model 2 remains quite lower than the experimental value. For G_{13} the value predicted by model 2 remains, up to $\psi \leqslant 40^\circ$, larger by a factor of 2–3 than the value predicted by model 1. A fair agreement is found in this case between model 2 and experimental results. For E_3 model 2 is stiffer than model 1 by a factor of about 2 but the experimental results remain underestimated.

Renewed interest has recently arisen on the mechanics of sandwich-type panels with cores consisting of a periodic assembly of struts (Evans et al., 2001; Deshpande and Fleck, 2001; Deshpande et al., 2001a; Wicks and Hutchinson, 2001; Chiras et al., 2002). Such "truss lattice" panels can be designed to present optimum stiffness to weight ratio. Deshpande et al. (2001b) have analysed the conditions under which pin-jointed truss lattices can present a completely stretching-dominated deformation behaviour (i.e. full triangulation).

As the stiffness of such lattices corresponds to the maximum achievable stiffness for a fibre network, it is instructive to compare the elastic constants predicted by models 1 and 2 with the elastic constants of a completely stretching-dominated truss lattice with the same volume fraction V_f. As reference for comparison, let us consider a sandwich core consisting of a single layer of pyramidal truss lattice sandwiched between two solid face-sheets at which the trusses are pin-jointed (the triangulation is thus provided by the face-sheets). As demonstrated by Deshpande and Fleck (2001), the values of E_3 and G_{13} for such a core express as

$$\frac{E_3}{E} = V_f \sin^4\psi \tag{22}$$

and

$$\frac{G_{13}}{E} = \frac{V_f}{8}\sin^2 2\psi \tag{23}$$

(the same expressions apply for a tetrahedral truss lattice). For E_3, the expression (22) does not depend whether four trusses meet at each node on the face-sheets, like in pyramidal lattices, or only two trusses meet at each node, like in interconnected fibre networks. For G_{13}, the expression (23) for pyramidal lattices apply for the case of two trusses meeting at each node only when the shear direction is parallel to one of the two in-plane fibre directions. Expressions (22) and (23) for $V_f = 0.2$ are presented as dot-dashed curves in Fig. 8. First, it can be noticed in Fig. 8b that the experimental value for E_3 is larger than the truss lattice E_3 value, which was anticipated to represent an upper bound. The reason is that the truss lattice model is based on the hypothesis of perfect pin-jointing at the nodes. In actual fibrous networks, the fibres segments do not behave like pin-jointed struts because free rotation at the nodes is prevented. In the case of E_3, the stiffening contribution due to the moments at the nodes increases when ψ decreases. As a result, for a network of interconnected fibres, E_3 does not tend to vanish when ψ tends towards zero, in contrast to the trend expressed by (22). Nevertheless, relations (22) and (23) may be considered as providing relevant estimates of E_3 and G_{13} for fully triangulated, stretching-dominated fibre networks, except at low ψ for E_3 and at high ψ for G_{13}. Fig. 8 shows that, at high ψ, the predictions of the two models for both E_3 and G_{13} are lower than the predictions of the truss lattice model. At low ψ, model 2 predictions are close to the truss lattice values and, for G_{13}, both curves tend to agree with experimental results.

Fig. 9 presents the variation as a function of ψ of the bounds for the out-of-plane Poisson ratio v_{13} derived from the two conditions (20) and (21) for $V_f = 0.20$ (only the lowest of the two upper bounds and

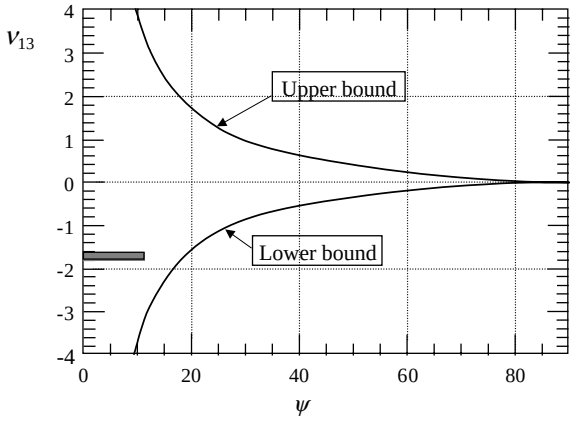

Fig. 9. Variation as a function of ψ of the bounds for the out-of-plane Poisson ratio v_{13} for $V_f = 0.20$. The rectangle in grey scale locates the v_{13} value measured for the reference material.

the highest of the two lower bounds are shown). The value of ν_{13} measured for the reference material is located in Fig. 9 in the form of a rectangle in grey scale. Obviously, the consideration of upper and lower bounds is not as informative for the Poisson ratios as for the other engineering elastic constants because these bounds span a very large range. Nevertheless, the curves predict that the possibility of a negative Poisson effect increases sharply as ψ decreases. The (largely negative) ν_{13} value measured for the reference material is found to be fully compatible with the model predictions.

4. Conclusion

The main objective underneath the present paper was to design a model that could account for two features of random planar fibre networks: the negative Poisson ratio behaviour and the random triangulation. Indeed, these features were not embedded in "model 1" developed by Delincé and Delannay (2004). The "model 2" proposed in this paper may be viewed as an extension in 3D of a 2D model for the elastic properties of honeycombs (Gibson and Ashby, 1997). This model can exhibit negative Poisson ratio behaviour in the three principal directions. It can thus correctly represent the behaviour of materials made of entangled fibres. The use of plates appears adequate for modelling the triangulation effect. However, the values of a and c to be used for the size of the plates, which determines the degree of triangulation, cannot be determined a priori. Comparison with experimental data suggests that the choice $a = a^*$ and $c = c^*$ with a^* and c^* defined by (3) and (4) is not unrealistic.

As expected, model 2 is generally stiffer than model 1. It follows that the predictions of model 2 for G_{13} appear to agree with the value measured for the reference material. This result is important because G_{13} is a major parameter for the design of sandwich cores. However, no such agreement is demonstrated for the predictions of E_1 and E_3 which remain significantly lower than experimental values. Nevertheless, although fully quantitative agreement with experiment is not demonstrated, the model can provide clues for orienting the design of the fibre orientation distribution that would provide the most adequate elastic anisotropy for the aimed application.

A major difficulty arises from the very low ψ angles characterising the reference material. Obviously, experimental data for random planar networks presenting higher average ψ angles should be obtained in order to better assess the two models. Conversely, different hypotheses or additional phenomena should be considered for accounting more accurately for the mechanisms governing the in-plane and out-of-plane stiffness at low ψ. Improved models should be designed in which fibres do not cross one another but are in contact along their external surface. These models should also account for the stiffening due to the possibility of squeezing of a fibre between two other fibres, a phenomenon that cannot occur when fibres cross one another along their symmetry axis. It should also be considered that a strain increment can cause some fibres to create a new contact, a mechanism that can affect the value of the Poisson ratio.

Acknowledgments

The author is indebted to M. Delincé and T. Pardoen for discussions and careful reading of the manuscript.

Appendix A. Influence of triangulation on the in-plane modulus E_1

Fig. A.1 sketches the architecture of a random network of fibres presenting a low out-of-plane angle ψ. Only 4 fibres segments meet at each node. These segments, which are assumed to be straight, form rings

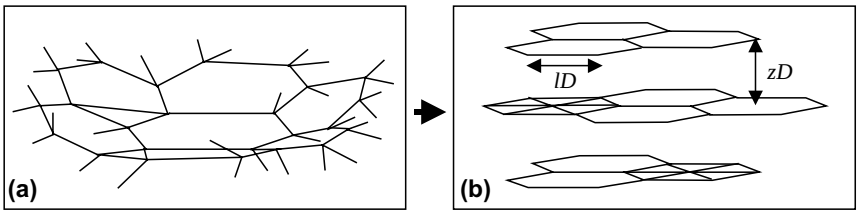

Fig. A.1. (a) Sketch of the architecture of a random fibre network containing mostly hexagonal and triangular rings; (b) representation of the network as a stacking of 2D nets of regular hexagons and triangles separated by a distance zD.

more or less parallel to the plane of isotropy. The number of segments of which these rings are actually made is variable. According to Gibson and Ashby (1997), in three-dimensional cellular structures, the number of edges per cell face is commonly close to 5.1. Hence, the fibre network is represented in Fig. A.1a as consisting of a combination of hexagonal and triangular rings: hexagonal rings account for the contribution of fibre bending to the in-plane compliance whereas triangular rings account for the contribution of triangulation. As a first approximation, it may be considered that the in-plane elastic properties derive primarily from the interconnections inside these rings, i.e. that the interconnections between rings in the $\boldsymbol{x}_3$ direction play only a minor role. Hence, as suggested in Fig. A.1b, the in-plane modulus E_1 of the actual structure can be estimated using, as a model, a stacking of two-dimensional nets made either of regular hexagons or of equilateral triangles, with constant distance $L = lD$ between the nodes. For any given relative proportion of hexagonal and triangular rings, the distance that separates these nets in the $\boldsymbol{x}_3$ direction can be derived from the actual network fibre volume fraction, V_f. The values of the in-plane moduli E_{1H} and E_{1T} for 2D nets containing only hexagons or only triangles, respectively, can then be calculated using the mechanics of honeycombs (e.g. Gibson and Ashby, 1997). One obtains

$$\frac{E_{1H}}{E} = \frac{9}{4} V_f \frac{1}{l^2} \tag{A.1}$$

and

$$\frac{E_{1T}}{E} = \frac{3}{4} V_f. \tag{A.2}$$

Using, as for the reference material, $V_f = 0.2$ and $l = 10$, relation (A.1) yields $E_{1H}/E = 4.5 \times 10^{-3}$ and relation (A.2) yields $E_{1T}/E = 150 \times 10^{-3}$. These values are, respectively, much lower and much higher than the value $E_1/E \approx 35 \times 10^{-3}$ that was experimentally measured by Delannay and Clyne (1999). It may thus be concluded that, in order to quantitatively predict the experimental values, the model must involve some degree of triangulation.

Appendix B. Derivation of the compliance matrix components S_{ij}

The analysis procedure being identical for the two models of Figs. 4 and 5, it will be illustrated only for the case of the model of Fig. 5. As represented in Fig. B.1, the elastic response of the RVE under normal stresses σ_{11}, σ_{22}, or σ_{33} can be fully characterised by considering only half of the segment AB together with a plate of size $aL/2 \times cL/2 \times t''L/2$. A simple force oriented along either of the three reference axes is applied on the middle of the fibre. Let us denote this force $\boldsymbol{p}_i = P\boldsymbol{x}_i$. By symmetry, no rotation at node A can occur for loading along $\boldsymbol{x}_1$. However, for loading along $\boldsymbol{x}_2$ or $\boldsymbol{x}_3$, the moment at the node has a component perpendicular to the plate, which induces an in-plane deformation of the plate. We neglect the effect of this

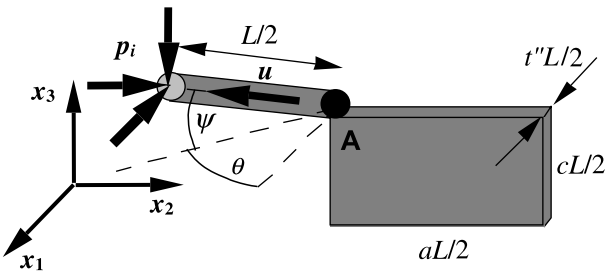

Fig. B.1. Representative element for characterising the elastic behaviour of the model of Fig. 5 under normal stresses σ_{11}, σ_{22} or σ_{33}.

moment and assume the absence of any rotation at the node for this configuration. Neglecting the contribution of shear, the relative displacement of the two nodes A and B at the ends of the fibre segment of length L is the sum of an axial stretching $\boldsymbol{v}_a$ and a bending deflection $\boldsymbol{v}_b$. Both displacements can easily be derived from elastic beam mechanics. The displacement Δ_{fi} in direction $\boldsymbol{x}_i$ of the load is obtained as the scalar product

$$\Delta_{fi} = (\boldsymbol{v}_a + \boldsymbol{v}_b) \cdot \boldsymbol{x}_i. \tag{B.1}$$

When loading along $\boldsymbol{p}_2$ or $\boldsymbol{p}_3$, the deformation of the two plates in the RVE also contributes to the deformation of the RVE. Even though we assume no in-plane rotation at the node, the plate deformation is not uniform. However, we approximate this deformation as equal to the deformation ε_{pij} of the plates under a uniform stress. The corresponding contributions Δ_{pi} to the relative displacement of the cell boundaries are thus easily obtained. For example, when loading the model of Fig. B.1 along $\boldsymbol{p}_2$,

$$\Delta_{p2} = \varepsilon_{p22} aL = \frac{4Pa}{Et''cL}. \tag{B.2}$$

Using (9) and (17), we have

$$t''c = \frac{\pi}{al^2}. \tag{B.3}$$

Hence

$$\Delta_{p2} = \frac{4Pl^2a^2}{E\pi L} = \frac{16l^4}{3\pi E}\frac{P}{L}\frac{3}{4}\frac{a^2}{l^2} \tag{B.4}$$

and

$$\Delta_{p3} = -v\varepsilon_{p22} cL = -v\frac{16l^4}{3\pi E}\frac{P}{L}\frac{3}{4}\frac{a^2 c}{l^2}. \tag{B.5}$$

Finally, the compliance tensor components S_{ij} with $i,j = 1$, 2 or 3 are obtained as

$$S_{ii} = \frac{1}{E_i} = \frac{\Delta_{fi} + \Delta_{pi}}{\sigma_{ii} X_i} \tag{B.6}$$

and

$$S_{ij} = -\frac{v_{ij}}{E_i} = \frac{\Delta_{fj} + \Delta_{pj}}{\sigma_{ii} X_j}, \tag{B.7}$$

where X_i is the size of the RVE in direction $\boldsymbol{x}_i$ (refer to Figs. 4 and 5). The stress components σ_{ij} are obtained from the $\boldsymbol{p}_i$ and the area of the corresponding RVE faces. The ensuing S_{ij} expressions are listed in Tables 1 and 2.

For obtaining the shear compliances S_{ii} with $i = 4$, 5, or 6, the response of the network of Fig. 5 under shear stresses τ_{12}, τ_{13} and τ_{23} can be characterised using the three representative elements sketched in Fig. B.2. For symmetry reasons, the middle of the fibres is under simple load (no bending moment) and no node rotation occurs under the shear stresses τ_{12}, τ_{13} (Fig. B.2a and b). We neglect the elastic rotation of the node that can occur in the plane of the plate under τ_{23} (Fig. B.2c). We adapt here for a 3D periodical model the procedure used by Gibson and Ashby (1997) for deriving the in-plane shear components of the stiffness matrix of a 2D honeycomb.

Equilibrium allows deriving the force on the middle of the fibres as the sum of two forces denoted $\boldsymbol{p}_i = P_i \boldsymbol{x}_i$ and $\boldsymbol{q}_{ij} = Q_{ij}\boldsymbol{x}_j$. Let us consider for example Fig. B.2a. The shear stress can be expressed either as

$$\tau_{12} = \frac{P_1}{L^2 \cos\psi \cos\theta (c + \sin\psi)} \tag{B.8}$$

or as

$$\tau_{12} = \frac{Q_{12}}{L^2 (a + \cos\psi \sin\theta)(c + \sin\psi)}. \tag{B.9}$$

Hence

$$Q_{12} = \frac{a + \cos\psi \sin\theta}{\cos\psi \cos\theta} P_1. \tag{B.10}$$

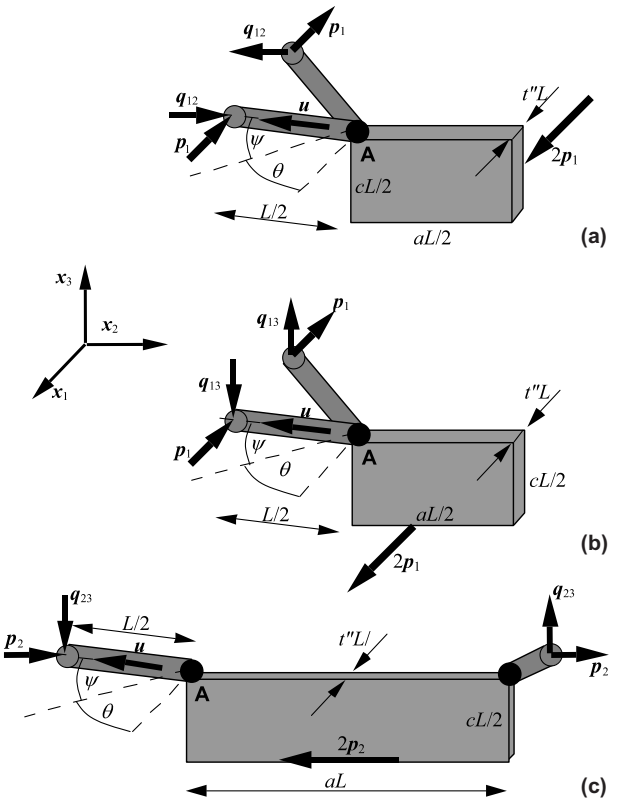

Fig. B.2. Three representative elements used for characterising the elastic behaviour of the model of Fig. 5 under shear stresses τ_{12} (a), τ_{13} (b), and τ_{23} (c).

The same procedure can be followed for deriving Q_{13} and Q_{23}.

The relative displacement of the middle of the fibres with respect to the node (i.e. over a length $L/2$) is the sum of a bending deflection $\boldsymbol{v}_{\mathrm{b}ij}$ and an axial stretching $\boldsymbol{v}_{\mathrm{a}ij}$, which can be derived from elastic beam mechanics.

The displacement $\boldsymbol{v}_{\mathrm{b}ij}$ of the middle of the fibre causes a rotation $\phi^{\mathrm{n}}_{\mathrm{b}ij}$ of the node around axis $\boldsymbol{x}_k$ (with $k \neq i, j$). In vectorial form, this rotation can be expressed

$$\phi^{\mathrm{n}}_{\mathrm{b}ij} = (\boldsymbol{u} \times \boldsymbol{v}_{\mathrm{b}ij}) \cdot \boldsymbol{x}_k. \tag{B.11}$$

The bending of the two fibres also results in a rotation ϕ^{p}_{ij} of the middle of the edge of the plate with respect to the middle of the line connecting the two points of application of the loads (middles of the two fibres supporting the plate). This rotation can be expressed as

$$\phi^{\mathrm{p}}_{ij} = \phi^{\mathrm{n}}_{\mathrm{b}ij} \frac{s_i}{X_i}, \tag{B.12}$$

where X_i is the size of the RVE in direction $\boldsymbol{x}_i$ and s_i is the size of the plate in direction $\boldsymbol{x}_i$, which is equal to aL or cL depending on the direction. ϕ^{p}_{ij} is zero when $s_i = 0$ i.e. when the plate is perpendicular to axis $\boldsymbol{x}_i$. Hence, due to the bending of the fibres, the middle of the plate shifts with respect to the middles of the fibres over a distance

$$\Delta_{\mathrm{b}ij} = \phi^{\mathrm{n}}_{\mathrm{b}ij} s_j - \phi^{\mathrm{p}}_{ij} X_j = \phi^{\mathrm{n}}_{\mathrm{b}ij} \left(s_j - s_i \frac{X_j}{X_i} \right). \tag{B.13}$$

One of the two fibres elongates while the other contracts. As represented in Fig. B.3, the result is a rotation of the plate by an angle $\phi^{\mathrm{p}}_{\mathrm{a}ij}$ plus a displacement of the node by a length $\Delta^{\mathrm{n}}_{\mathrm{a}i}$. $\phi^{\mathrm{p}}_{\mathrm{a}ij}$ and $\Delta^{\mathrm{n}}_{\mathrm{a}i}$ can be derived, from consideration of Fig. B.3, as

$$\phi^{\mathrm{p}}_{\mathrm{a}ij} = \frac{2(\boldsymbol{v}_{\mathrm{a}ij} \cdot \boldsymbol{x}_j)}{X_i} \tag{B.14}$$

and

$$\Delta^{\mathrm{n}}_{\mathrm{a}i} = \boldsymbol{v}_{\mathrm{a}ij} \cdot \boldsymbol{x}_i. \tag{B.15}$$

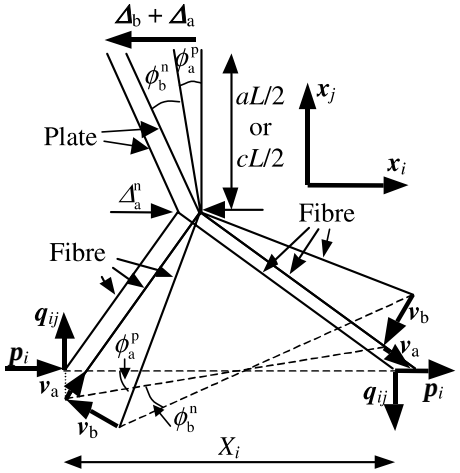

Fig. B.3. Rotation and displacement of the plate as a result of the bending and elongation/contraction of the two fibres.

The total displacement Δ_{aij} of the middle of the plate (with respect to the middle of the fibres) resulting from the axial elongation of the fibres is then obtained as

$$\Delta_{aij} = \phi^{p}_{aij} s_j + \Delta^{n}_{ai}. \tag{B.16}$$

Figs. B.2a and b indicate that the deflection of the plate under the shear stresses τ_{12} or τ_{13} adds a further contribution to the deformation of the RVE. For example, under τ_{12} (Fig. B.2a), the deflection Δ^{p}_{12} of the middle of the plate with respect to the node writes (neglecting the contribution due to shear)

$$\Delta^{p}_{12} = \frac{2Pa^3}{ELct''^3} \tag{B.17}$$

which, using (9) and (B.3) translates into

$$\Delta^{p}_{12} = \frac{8Pl^4}{3\pi EL}\frac{3a^4 c}{4\pi V_f}. \tag{B.18}$$

In the case of a shear stress τ_{23} (Fig. B.2c), the plate undergoes no bending but only in-plane shear (that may be non-negligible in comparison to the other contributions for certain values of ψ and θ). The displacement of the middle of the plate with respect to the node writes

$$\Delta^{p}_{23} = \frac{2Pc}{\mu Lat''}, \tag{B.19}$$

where μ is the shear modulus of the fibres. Using $\mu = 3E/8$ allows deriving

$$\Delta^{p}_{23} = \frac{8Pl^4}{3\pi EL} 2\frac{c^2}{l^2}. \tag{B.20}$$

Finally, the shear compliances S_{ii} with $i = 4$, 5 or 6 are obtained as, for example

$$S''_{66} = \frac{1}{G_{12}} = \frac{\gamma_{12}}{\tau_{12}} = \frac{2(\Delta_{b12} + \Delta_{a12} + \Delta^{p}_{12})LX''_1 X''_3}{PX''_2}. \tag{B.21}$$

References

Ashby, M.F., Evans, A.G., Fleck, N.A., Gibson, L.J., Hutchinson, J.W., Wadley, H.N.G., 2000. Metal Foams, A Design Guide. Butterworth Heinemann, Stoneham, MA.

Chiras, S., Mumm, D.R., Evans, A.G., Wicks, N., Hutchinson, J.W., Dharmasena, K., Wadley, H.N.G., Fichter, S., 2002. The structural performance of near-optimized truss core panels. Int. J. Solids Struct. 39 (15), 4093–4115.

Delannay, F., 1998. Elastic and plastic properties of mats of sintered fibres. In: Proceedings Colloque National de Métallurgie des Poudres, Société Française de Métallurgie et des Matériaux, Nanterre, France, pp. 351–356.

Delannay, F., Clyne, T.W., 1999. Elastic properties of cellular metals processed by sintering mats of fibres. In: Banhart, J., Ashby, N.A., Fleck, N.A. (Eds.), Metal Foams and Porous Metal Structures. MIT-Verlag, Bremen, Germany, pp. 293–298.

Delincé, M., Delannay, F., 2004. Elastic anisotropy of a transversely isotropic random network of interconnected fibres: non triangulated network model. Acta Mater. 52, 1013–1022.

Deshpande, V.S., Fleck, N.A., 2001. Collapse of truss core sandwich beams in 3-point bending. Int. J. Solids Struct. 38, 6275–6305.

Deshpande, V.S., Fleck, N.A., Ashby, M.F., 2001a. Effective properties of the octet-truss lattice material. J. Mech. Phys. Solids 49, 1747–1769.

Deshpande, V.S., Ashby, M.F., Fleck, N.A., 2001b. Foam topology bending versus stretching dominated architectures. Acta Mater. 49, 1035–1040.

Evans, K.E., Nkansah, M.A., Hutchinson, I.J., 1994. Auxetic foams: modelling negative Poisson's ratios. Acta Metall. Mater. 42 (4), 1289–1294.

Evans, A.G., Hutchinson, J.W., Fleck, N.A., Ashby, M.F., Wadley, H.N.G., 2001. The topological design of multifunctional cellular metals. Progress Mater. Sci. 46, 309–327.

Friis, E.A., Lakes, R.S., Park, J.B., 1988. Negative Poisson's ratio polymeric and metallic foams. J. Mater. Sci. 23, 4406–4414.
Gibson, L.J., Ashby, M.F., 1997. Cellular Solids. Cambridge University Press.
Gommers, B., Verpoest, I., Van Houtte, P., 1996. Modelling the elastic properties of knitted-fabric-reinforced composites. Compos. Sci. Technol. 56, 685–694.
Kolpakov, A.G., 1985. On the determination of averaged moduli of elastic gridworks. Prikl. Mat. Mekh. 59, 969–977.
Lakes, R.S., 1987. Foam structures with a negative Poisson's ratio. Science 235, 1038–1040.
Lakes, R.S., 1991. Deformation mechanisms of negative Poisson's ratio materials: structural aspects. J. Mater. Sci. 26, 2287–2292.
Milton, G., 1992. Composites materials with Poisson's ratio close to −1. J. Mech. Phys. Solids 40, 1105–1137.
Mura, T., 1982. Micromechanics of defects in solids. Martinus Nijhoff, The Hague, pp. 368–370.
Nye, J.F., 1985. Physical Properties of Crystals. Oxford University Press.
Overaker, D.W., Cuitino, A.M., Langrana, N.A., 1998a. Elastoplastic micromechanical modelling of two-dimensional irregular convex and non-convex (re-entrant) hexagonal foam. J. Appl. Mech. 65 (3), 748–757.
Overaker, D.W., Cuitino, A.M., Langrana, N.A., 1998b. Effects of morphology and orientation on the behaviour of two-dimensional hexagonal foams and application in a re-entrant foam anchor model. Mech. Mater. 29 (1), 43–52.
Rothenburg, L., Berlin, A.A., Bathurst, R.J., 1991. Microstructure of isotropic materials with negative Poisson ratio. Nature 354, 470–472.
Schajer, G.S., Robertson, C.I., 1974. Mechanical behaviour of cellular structures. Project report, Pembroke College, Cambridge University.
Wicks, N., Hutchinson, J.W., 2001. Optimal truss plates. Int. J. Solids Struct. 38, 5165–5183.